Comparative Investigation of Torque-ripple Suppression Control Strategies Based on Torque-sharing Function for Switched Reluctance Motor

Tong Chen, and Guoyang Cheng

***Abstract*—Torque ripple is an inherent property of switched reluctance motor (SRM), which seriously affects the control performance and application of the motor. This paper proposes two torque ripple suppression control strategies based on torque-sharing function (TSF). According to the symmetry characteristics of the flux linkage and rotor position curve family, a fourth-order Fourier series is used to fit the SRM flux linkage analytical model. The coefficient of each harmonic term of the flux linkage model is a function related to current, expressed by a sixth-order polynomial. The torque analytical formula can be derived from the flux linkage model. The torque error is calculated via the identified torque model and is compensated through TSF controller in order to reduce torque ripple. The torque model can also be used to establish the torque loop to achieve accurate tracking of the TSF reference torque to reduce torque ripple. Digital simulation was conducted, followed by the implementation on a SRM test bench using a 28335DSP as the master control chip. The experimental results are consistent with the simulation results, and indicate the effectiveness of the proposed schemes.**

***Index Terms*—Switched reluctance motor, analytical model, torque ripple suppression, torque-sharing function (TSF).**

I. Introduction

As a new generation of drive motor, switched reluctance motor (SRM) has a simple structure, high operating efficiency and high reliability without winding on the rotor side. Such advantages enable it to be widely used in electric vehicles, textile machinery, mining, oil fields, aerospace industry, and other industry applications [1]-[3]. Due to the unique double salient structure and the pulsed power supply mode of SRM, the torque ripple, noise and vibration of the motor are relatively large. This poses a challenge for high-performance applications, and has inspired a sustained research interest in suppressing the torque ripple in SRM.

Manuscript received June 14, 2021; revised September 08, 2021, and November 15, 2021; accepted December 21, 2021. date of publication June 25, 2022; date of current version June 18, 2022.

This work was supported in part by National Natural Science Foundation of China under Grant 51977040.(*Corresponding Author: Guoyang Cheng*)

Tong Chen and Guoyang Cheng are with the College of Electrical Engineering and Automation, Fuzhou University, Fuzhou, 350108 China (e-mail: 1184477056@qq.com, cheng@ fzu.edu.cn).

Digital Object Identifier 10.30941/CESTEMS.2022.00023

The torque sharing function (TSF) can reduce the torque ripple generated during commutation by distributing the torque among each phase of the motor. However, as the speed of the motor increases, the phase current of the motor cannot accurately track the reference current, resulting in torque ripple. By optimizing TSF structure or compensation current, SRM can suppress torque ripple in a wide speed range. A neuro-fuzzy compensator is proposed in [4] to generate compensating current signals to reduce torque ripple. Choi *et al* expands the working range of TSF from the original first quadrant to the second quadrant, so that the system can also obtain a larger torque when running at high speed, and reduce the torque ripple of SRM in a wider speed range [5]. In [6], a series of TSF optimization methods to reduce the torque ripple and copper loss are presented, and a novel family of TSFs is introduced. In [7], the commutation interval is divided into two parts, and the compensation current will be added to the corresponding phase reference current in different intervals so as to reduce the torque ripple. The iterative learning controller is used to add the compensation current to the reference current in [8]. In [9], genetic algorithm is used to optimize the opening angle and the overlap angle of TSF to obtain the desired torque, and to maximize the speed range and reduce the copper loss. In [10], the opening angle of SRM is adapted online without adjusting the structure of TSF. In [11], [12], the reference current waveform is planned through a series of methods to reduce the torque ripple. A new TSF method is proposed in [13], which achieves lower current tracking error by adjusting the current reference value through an optimization function.

After the expected torque of each phase is obtained via TSF, the direct instantaneous torque control (DITC) with torque closed-loop can also be used to track the expected torque, but it calls for an accurate torque model. Using the bicubic spline method to establish a flux linkage model requires a large amount of flux linkage-rotor position-phase current data to ensure the accuracy of the model [14]. In [15], a Gaussian function is proposed to fit the saturation region of the flux linkage data such that the accuracy of the model is improved, but the torque calculation is difficult. The Fourier-series is used to establish the flux linkage model in [16] and [17]. In [18], on the basis of the fourth-order Fourier series model data, the

Kriging model is used to improve the accuracy of modeling. In [19], a nonlinear analytical model of inductance based on Gaussian distribution probability density function is proposed, but the torque model has a poor accuracy. The method of using two dimensional orthogonal polynomials to simulate magnetic characteristics is proposed in [20].

In this paper, the least square method is used to identify the parameters of the flux linkage model based on the Fourier-series, and a simplified torque formula can be obtained. Then, the torque model will be utilized to develop two control strategies for torque ripple suppression, one is the torque compensation control strategy which compensates the torque error via the TSF controller, and the other is the DITC strategy using torque closed-loop regulation. The DITC strategy is found to be effective in suppressing torque ripple, as will be verified by analyzing the performances of the two control strategies mentioned above. In the research of torque ripple suppression, DITC may emerge as a direction of great promise.

The rest of this paper is organized as follows. The torque model is presented in Section II. In Section III, the torque compensation control strategy and the direct instantaneous torque control strategy are introduced. Section IV presents the simulation verification of the two control schemes and their implementation on a switched reluctance drive system. Finally, some concluding remarks can be found in Section V.

II. MODELING OF SRM

In this section, the torque model of SRM will be determined. The model is based on a 3-phase, 6/4 structure SRM experimental motor with a rated voltage of 50V and a rated power of 250W.

A. Modeling of Nonlinear Magnetic Characteristics

In this paper, the model is based on the flux linkage-rotor position curve family $(\psi-\theta)$, and a better fitting effect is obtained with the help of the curve symmetry. Fig.1 shows the flux linkage-rotor position-phase current curve family $(\psi-\theta)$ of a certain phase of the experimental SRM obtained by the FEA (finite element analysis) method. The non-aligned position of the salient poles of the stator and the rotor is set to 0°, and the aligned position is set to 45°.

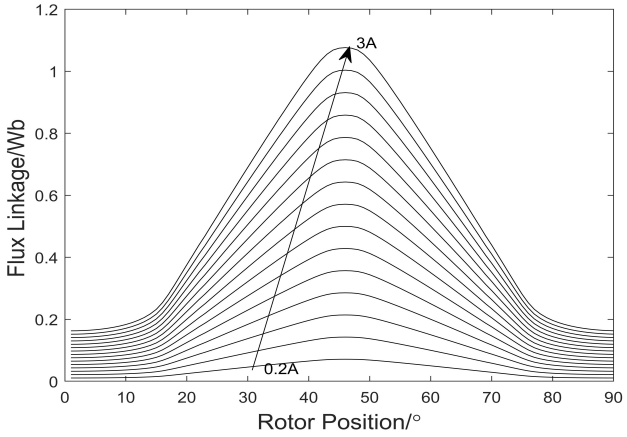

Fig. 1.The $\theta-i$ curve family of different rotor positions.

The flux linkage versus rotor position curve has symmetrical characteristics and periodicity, and its symmetrical characteristics require that the analytical model be an even function. So, the combination of multiple cosine functions are used to express such a rich family of curves. The combination of multiple functions to form a complete orthogonal function is exemplified by the Fourier series [16]. Taking into account the calculation efforts and fitting accuracy, equation (1) is selected to express the single phase flux linkage model. The formula includes some constants and 1 to 4 harmonics.

$$\psi(\theta,i)=\sum_{\mathrm{n}=0}^{4}a_{\mathrm{n}}(i)\cos(\mathrm{n}\omega\theta) \tag{1}$$

where ω is the angular frequency, and its value is related to the structure of the motor. In this paper, $\omega=4\pi/180$. Hence, equation (1) can be expanded to get:

$$\begin{aligned}\psi(\theta,i)=a_0+a_1\cos(\frac{4\pi}{180}\theta)+a_2\cos(\frac{8\pi}{180}\theta)\\+a_3\cos(\frac{12\pi}{180}\theta)+a_4\cos(\frac{16\pi}{180}\theta)\end{aligned} \tag{2}$$

where a_0 to a_4 are the coefficients related to the phase current, θ is the rotor position angle. The model identification is completed in two steps. Firstly, the flux linkage data obtained through FEA are used to fit the analytical relationship between flux linkage and rotor position, as given by equation (2). Specifically, the least square method based on Levenberg-Marquardt algorithm, i.e., the function lsqcurvefit() in the MATLAB nonlinear function fitting toolbox, is chosen to fit the flux linkage data, so as to identify the coefficients a_0 to a_4. The identification results are shown in Table I.

Secondly, the coefficients a_0 to a_4 are related to the phase current. To trade off between accuracy and computation, each of the above coefficients is expressed by a 6th-order polynomial as in (3) that is easy to be calculated by Qin Jiushao's algorithm.

$$a_n=\sum_{\mathrm{j}=0}^{6}c_{\mathrm{nj}}i^{\mathrm{j}},\ \mathrm{n}=0,1,2,3,4. \tag{3}$$

where c_{nj} is the coefficient of each term in a_{n}. Using the same identification method, the values of these coefficients are

TABLE I
COEFFICIENT a_0 TO a_3

i/A	a_0	a_1	a_2	a_3	a_4
0.2	0.03651	-0.03007	0.00445	0.000121	0.001234
0.4	0.07113	-0.06006	0.008938	0.0002535	0.002454
0.6	0.1067	-0.09009	0.01337	0.000378	0.003679
0.8	0.1423	-0.1201	0.01788	0.000503	0.04909
1.0	0.1778	-0.1502	0.02235	0.0006625	0.006133
1.2	0.2134	-0.1802	0.02683	0.0007478	0.007362
1.4	0.249	-0.2103	0.03131	0.0008652	0.008594
1.6	0.2846	-0.2403	0.03581	0.000977	0.009828
1.8	0.3202	-0.2704	0.04032	0.001072	0.0107
2.0	0.3558	-0.3006	0.04487	0.001159	0.01232
2.2	0.3915	-0.3308	0.04946	0.001221	0.01358
2.4	0.4273	-0.3611	0.0541	0.001251	0.01486
2.6	0.463	-0.3915	0.05879	0.001257	0.01615
2.8	0.4988	-0.422	0.06353	0.001249	0.01744
3.0	0.5347	-0.4525	0.06828	0.001243	0.01872

identified and shown in Table II. So far, the flux linkage model of the experimental motor has been completely established, as given by equations (2) and (3) together with the coefficients in Table II.

TABLE II
COEFFICIENT c_{NJ}

c_{nj}	a_0/Wb	a_1/Wb	a_2/Wb	a_3/Wb	a_4/Wb
c_{n0}	-1.216e-5	5.389e-5	-2.724e-5	1.419e-5	-1.122e-5
c_{n1}	1.088e-4	-4.414e-4	2.309e-4	-1.091e-4	8.878e-5
c_{n2}	-3.561e-4	1.289e-3	-7.304e-4	2.947e-4	-2.574e-4
c_{n3}	6.207e-4	-1.761e-3	1.195e-3	-3.778e-4	3.617e-4
c_{n4}	-5.316e-4	1.087e-3	-1.047e-3	2.203e-4	-2.407e-4
c_{n5}	0.178	-0.1504	2.281e-2	5.846e-4	6.192e-3
c_{n6}	6.203e-6	-6.006e-6	-7.819e-5	-3.984e-7	5.54e-7

B. Torque Calculation

In the past, approximate functions were applied in modeling to reduce the computational complexity when calculating the motor torque. For example, in order to approximate the non-integrable part, the hyperbolic tangent function was introduced in [15], which would cause new calculation errors. In contrast, the method we adopt here does not require function approximation.

The torque of a certain phase (indexed by k) of the motor can be derived from the magnetic co-energy W:

$$T_k(i_k,\theta)=\frac{\partial W}{\partial \theta}=\frac{\partial}{\partial \theta}\int_0^{i_k}\psi_k di \tag{4}$$

where i_k is the phase instantaneous current. Substitution of (2) into (4) yields

$$\begin{aligned}T_k=&-\frac{4\pi}{180}\sin(\frac{4\pi}{180}\theta)\int a_1(i)di-\frac{8\pi}{180}\sin(\frac{8\pi}{180}\theta)\int a_2(i)di\\&-\frac{12\pi}{180}\sin(\frac{12\pi}{180}\theta)\int a_3(i)di-\frac{16\pi}{180}\sin(\frac{16\pi}{180}\theta)\int a_4(i)di\end{aligned} \tag{5}$$

where coefficient $a_n(i)$ is the sixth-order polynomial in equation (3), so $\int a_n(i)di$ is completely integrable. Fig.2 shows the torque waveforms produced by the torque model under different phase currents, and the results are fairly consistent with the torque data obtained by FEA simulation.

III. Torque Ripple Suppression Schemes

In this section, two control schemes for suppressing torque ripple based on TSF strategy will be presented.

A. Torque Compensation Strategy Based on TSF

The torque T_k produced by the k-th phase of SRM is related to the phase current and the change rate of phase inductance $L_k(i,\theta)$ versus rotor position, as follows:

$$T_k=\frac{1}{2}i^2\frac{\partial L_k(i,\theta)}{\partial \theta} \tag{6}$$

From equation (6) it is clear that the generated torque is dependent on the phase current and the inductance's change rate. In general, when SRM is in commutation, the torque of the outgoing phase begins to decline, and the current of the incoming phase is not fully established and results in a small torque, hence a torque drop will occur. At the position where the salient poles of the stator and rotor are completely aligned and the position where the salient poles of the stator and the rotor groove are aligned, the phase inductance's change rate is the lowest, so the torque generated at these two positions are the smallest. During the spell of phase commutation, the two adjacent phases are close to the above two positions respectively, and neither phase can provide a large torque. As a result, the torque ripple of SRM is particularly significant upon the phase commutation.

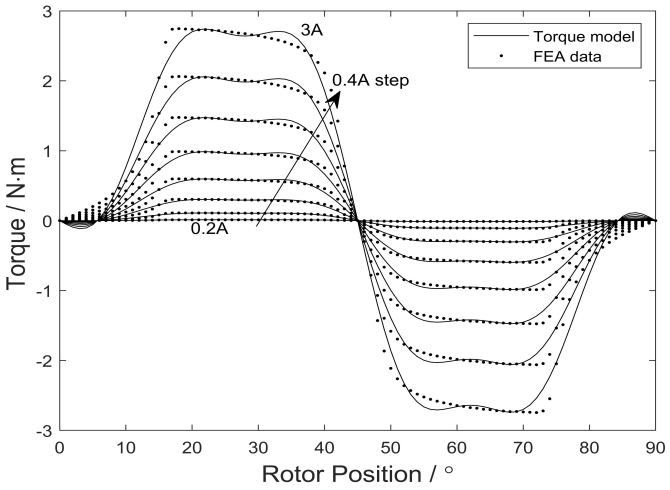

Fig.2. Comparison of torques between the proposed model and the FEA data.

Using the torque-sharing function (TSF) can effectively suppress the torque ripple caused by the motor's commutation action. Taking the effect of copper loss into account, the sinusoidal TSF in [9] is adopted here, as shown in Fig.3.

In a rotor period τ_r, the reference instantaneous torque $T_k(\theta)$ of the k-th phase can be expressed as:

$$T_k(\theta)=\begin{cases}0, & 0\le\theta\le\theta_{on}\\ T_{ref}\cdot f_{rise}(\theta), & \theta_{on}<\theta\le\theta_{on}+\theta_{ov}\\ T_{ref}, & \theta_{on}+\theta_{ov}<\theta\le\theta_{off}\\ T_{ref}\cdot f_{fall}(\theta), & \theta_{off}<\theta\le\theta_{off}+\theta_{ov}\\ 0, & \theta_{off}+\theta_{ov}<\theta\le\tau_r\end{cases} \tag{7}$$

where

$$f_{rise}(\theta)=0.5-0.5\cos(\pi\frac{\theta-\theta_{on}}{\theta_{ov}}) \tag{8}$$

$$f_{fall}(\theta)=0.5+0.5\cos(\pi\frac{\theta-\theta_{off}}{\theta_{ov}}) \tag{9}$$

The block diagram of the traditional indirect torque control strategy is shown in Fig.4. A speed controller is designed to produce the reference total torque T^*, and the TSF is used to distribute the total torque to each phase T_{ph}^*, then the reference phase current i_{ph}^* is obtained via the inverse torque model $i(T,\theta)$. Finally, the current controller is adopted to regulate the feedback current towards its reference target.

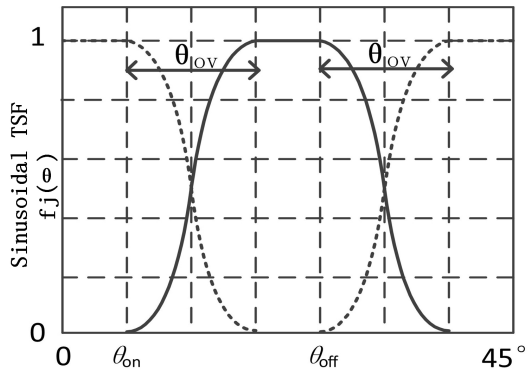

Fig.3. Sinusoidal TSF.

However, the actual torque output in Fig.4 is determined by the current tracking performance. Limited by the DC bus voltage, the actual motor current cannot accurately track the reference current, therefore, the torque ripple may still exist. The error of current tracking mostly appears in the demagnetizing period when the motor has a higher inductance value. For that reason, a torque compensation strategy based on modified TSF is adopted in this paper as shown in Fig.5.

The output of the speed controller is a torque instruction that represents the total reference torque of the system. The real-time total torque of the switched reluctance drive is calculated by the torque model determined in the section II. The torque error ΔT can be obtained by subtracting the real-time total torque from the reference total torque, and then compensated by the TSF controller. The new TSF is expressed by (10).

$$T_k(\theta)=\begin{cases}0, & 0\le\theta\le\theta_{on}\\ T_{ref}\cdot f_{rise}(\theta)+\Delta T, & \theta_{on}<\theta\le\theta_{on}+\theta_{ov}\\ T_{ref}+\Delta T, & \theta_{on}+\theta_{ov}<\theta\le\theta_{off}\\ T_{ref}\cdot f_{fall}(\theta), & \theta_{off}<\theta\le\theta_{off}+\theta_{ov}\\ 0, & \theta_{off}+\theta_{ov}<\theta\le\tau_r\end{cases} \quad (10)$$

The torque error is compensated by the incoming phase. This torque compensation strategy is also applicable to other types of torque- sharing function.

In the actual digital control system, the output of the hysteresis controller will lag behind the change of the reference current, and the actual current cannot accurately track the reference current, resulting in torque ripple. Therefore, the fixed-frequency PWM control is used in the current loop to replace the traditional hysteresis controller in this paper, and an incremental PID control algorithm is adopted. The output of the algorithm is the increment of the control signal. When the system is heavily disturbed, the algorithm will not seriously degrade the operation of the system, so it has better robustness.

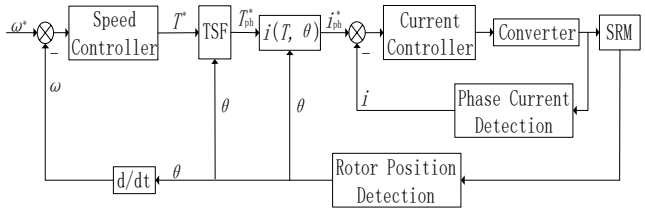

Fig.4. Block diagram of the indirect torque control scheme.

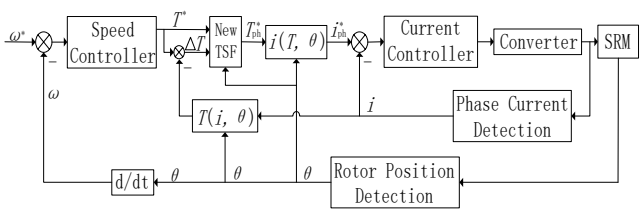

Fig.5. Block diagram of the torque compensation scheme.

B. Direct Instantaneous Torque Control

Another scheme for suppressing torque ripple will be presented in this subsection. The indirect torque control strategy must convert the reference torque command into a reference current command, and there is no torque closed loop in the control system. However, it is more difficult to convert the reference torque command accurately into the reference current command, which is also a cause of torque ripple. The DITC strategy does not need to convert the desired torque into an equivalent desired current, and can directly control the torque, so the torque response is faster. The DITC is a simple and effective control method. Compared with indirect torque control, the control of the current loop is omitted in DITC, and the torque difference is used to realize the precise tracking of the TSF more directly.

To achieve direct instantaneous torque control, torque feedback is essential. The torque feedback in this paper is obtained by the torque model $T(i,\theta)$ identified in the previous section. This method does not need to install a torque sensor and is widely used. However, the torque ripple of the direct instantaneous torque control strategy is greatly affected by the accuracy of the torque model. The block diagram of SRM with DITC based on TSF technique is shown in Fig.6.

The fixed-frequency PWM control is used in the torque loop to replace the traditional hysteresis controller so as to reduce torque tracking error and torque ripple in this paper.

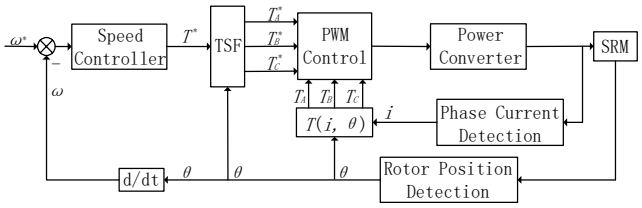

Fig.6. Block diagram of the DITC scheme.

IV. SIMULATION AND EXPERIMENTAL VERIFICATION

In this section, simulation and experimental verification of the torque compensation control strategy and the direct instantaneous torque control strategy will be conducted respectively, and a comparison will be made with the traditional indirect torque control strategy. The physical data of the SRM are shown in Table III.

A. Simulation Result

The indirect torque control strategy and the torque compensation control strategy adopts the traditional current loop control, using the data obtained by FEA to construct the current look-up table. Setting the load torque of SRM to

TABLE III
MOTOR DATA OF THE 6/4-POLE SRM

Parameter	*Value*
Stator diameter	80mm
Rotor diameter	41mm
Stack length	85mm
Air gap length	0.5mm
Stator pole arc	27°
Rotor pole arc	31.5°
Number of turns of phase winding	80

$0.4\ N\cdot m$. The phase inductance of switched reluctance motor varies periodically with rotor position. The angle when the front edge of the rotor overlaps with the rear edge of the stator can be calculated by combining with the structural parameters of the motor as 15.75°. And the angle when the front edge of the rotor overlaps with the front edge of the stator is 42.75°. The opening angle must be less than 15.75° to ensure sufficient current rise time. The turn-off angle must be less than 42.75° to ensure that the current drops to 0 when the phase inductance enters the drop zone. In a rotor period τ_r, the three phases must be staggered by 30° ($\theta_{off}-\theta_{on}$=30°) in order to ensure that the sum of the three phases' TSFs at any rotor position is 1. The opening angle and the turn-off angle cannot be determined by the explicit relation. By analyzing the results of different experiments, we set the opening angle θ_{on}=5°, the overlap period θ_{ov}=9° and the turn-off angle θ_{off}=35°.

The parameters of the PI speed controller are set to k_P=0.3, k_I=0.12 and the parameters of the current controller are set to k_P=100, k_I=50. Fig.7 and Fig.8 present the phase current, phase torque and total torque waveforms under the indirect torque control strategy and the torque compensation control strategy at 500RPM, respectively. The current waveform of a certain phase of SRM under the two control strategies is shown in Fig.9 at 500RPM. Figs.10~12 show the simulation results of the two control strategies at 1000RPM.

The torque compensation scheme converts the torque compensation into the reference current compensation through the inverse torque model, thereby reducing the current ripple, and achieving the effect of reducing the torque ripple as shown in Fig.8 and Fig.11.

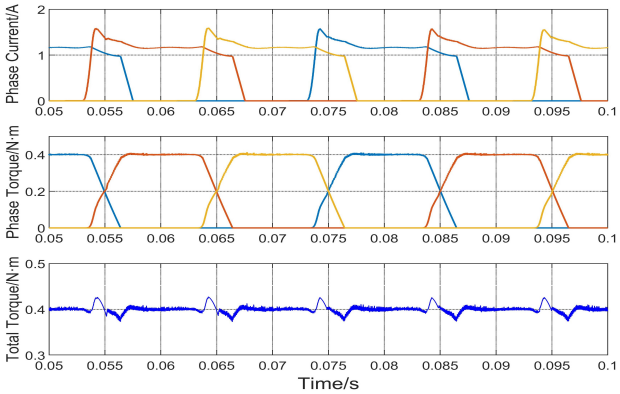

Fig.7. Phase current, phase torque and total torque waveform under indirect torque control (500RPM).

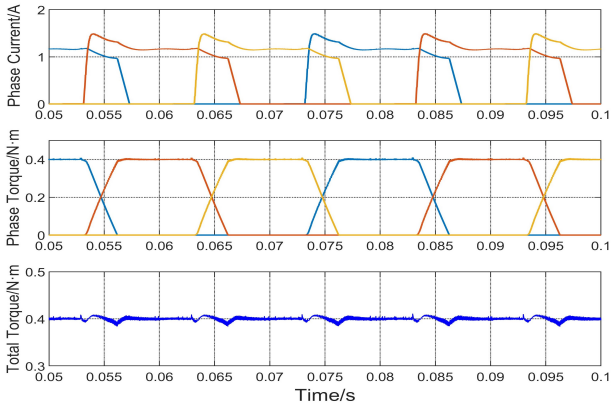

Fig.8. Phase current, phase torque and total torque waveform under torque compensation control (500RPM).

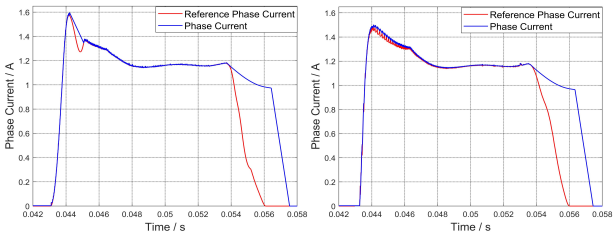

(a) (b)

Fig.9. A-Phase current waveform at 500RPM, (a):indirect torque control; (b): torque compensation control

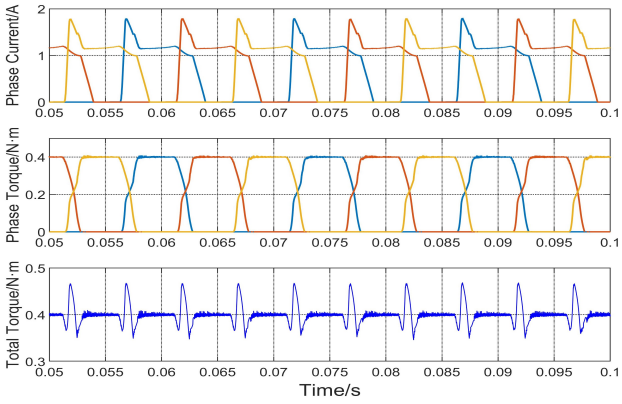

Fig.10. Phase current, phase torque and total torque waveform under indirect torque control (1000RPM).

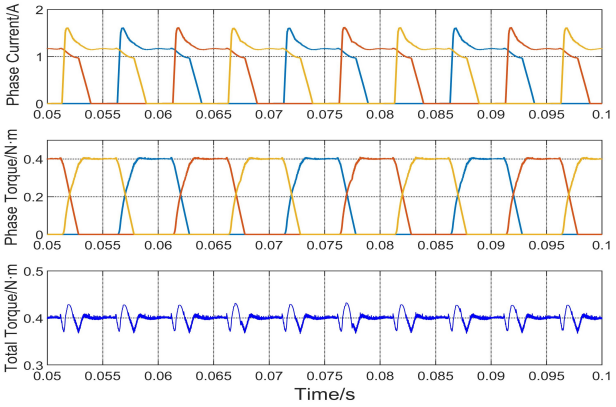

Fig.11. Phase current, phase torque and total torque waveform under torque compensation control (1000RPM).

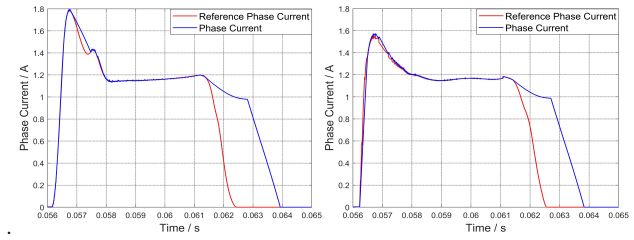

(a) (b)

Fig.12. A-Phase current waveform at 1000RPM, (a):indirect torque control; (b): torque compensation control

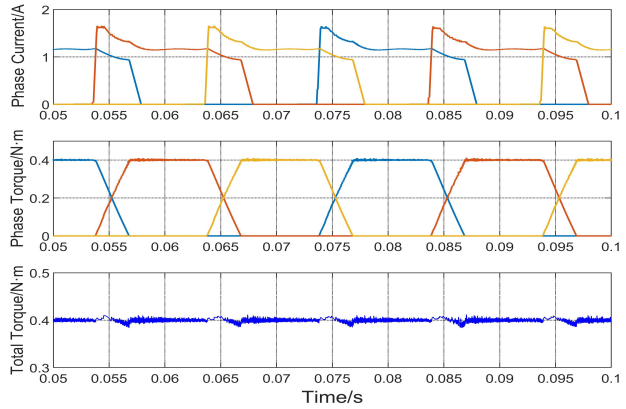

Fig.13. Phase current, phase torque and total torque waveform under DITC (500RPM)

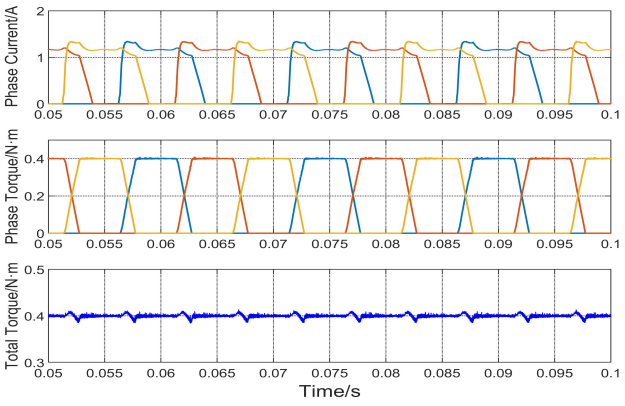

Fig.14. Phase current, phase torque and total torque waveform under DITC (1000RPM).

For the direct instant torque control scheme, we also set the load torque of SRM to 0.4 $N \cdot m$, and set the opening angle θ_{on}=5° , the overlap period θ_{ov}=9° and the turn-off angle θ_{off}=35° . The parameters of the PI speed controller are set to k_P=0.3, k_I=0.12 and the parameters of the current controller are set to k_P=80, k_I=25. Fig.13 and Fig.14 present the waveforms of phase current, phase torque and total torque when the reference speed is 500RPM and 1000RPM respectively. The torque waveform of the three control strategies at the reference speed of 1000RPM (load step from 0.4 $N \cdot m$ to 0.8 $N \cdot m$) are shown in Fig. 15.

Torque ripple rate can directly reflect the magnitude of torque pulsation during SRM operation. It refers to the ratio of the maximum amplitude of the total torque fluctuation to the average torque when the motor is running. Its expression is as follows:

$$K_T = \frac{T_{max} - T_{min}}{T_{avg}} \times 100\% \quad (11)$$

where T_{max} , T_{min} and T_{avg} are the maximum, minimum and average values of the total torque respectively. Table IV shows the torque ripple rate of the three control methods at different speeds.

The simulation results verify the effectiveness and robustness of the direct instantaneous torque control strategy and the torque compensation control strategy in suppressing torque ripple.

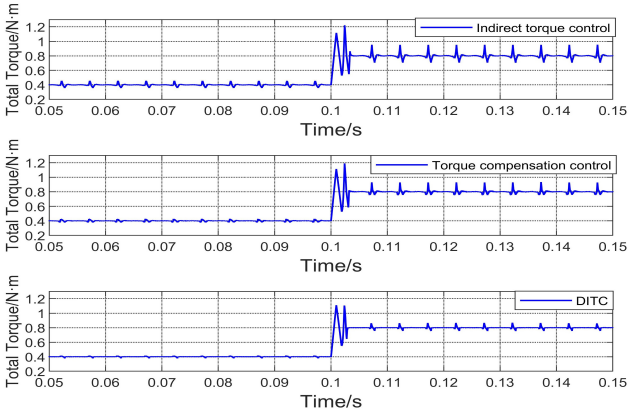

Fig.15. Total torque waveform of the three control strategies at 1000RPM (load step from 0.4 $N \cdot m$ to 0.8 $N \cdot m$)

TABLE IV
PERFORMANCE COMPARISON OF THE THREE CONTROL METHODS IN THE SIMULATION

RPM / $N \cdot m$	*Control Method*	*Torque Ripple Rate (%)*
500 / 0.4 $N \cdot m$	Indirect torque control	13.78
	Torque compensation control	6.85
	DITC	7.05
1000/ 0.4 $N \cdot m$	Indirect torque control	30.41
	Torque compensation control	16.57
	DITC	10.25
1000/ 0.8 $N \cdot m$	Indirect torque control	30.58
	Torque compensation control	21.55
	DITC	13.45

B. *Experiment Result*

Fig.16 shows the setup of the SRM test bench. The motor in the experiment is a three-phase 6/4-pole SRM, with a rated voltage of 50V, the rated power of 250W, and the phase resistance of 1.98 Ω. A 28335DSP from TI is adopted as the master control chip of the test bench. The power converter is a three-phase asymmetric half-bridge circuit. The driving circuit adopts the upper bridge arm bootstrap driving circuit, which can reduce the switching frequency of the switching device. The bootstrap capacitor needs time to charge up to the voltage level required for driving, so the frequency of PWM is set to 10KHz. The same frequency is used for torque control.

In addition, a combination of soft chopping and hard chopping is adopted as the chopping mode of the power device.

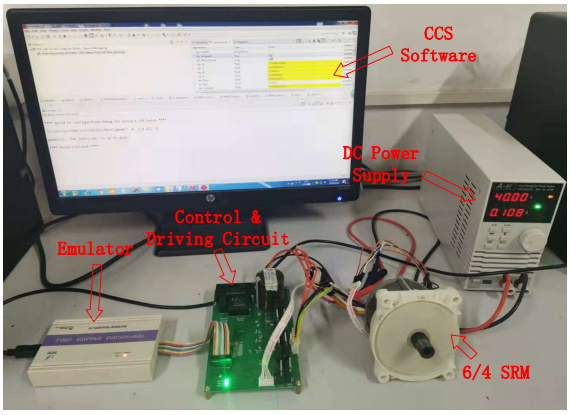

Fig.16. SRM test bench.

When the rotor position is between the opening angle θ_{on} and the turn-off angle θ_{off}, the power device adopts soft chopping, and the lower bridge arm is always on, while the upper bridge arm changes the on-off state according to the duty cycle. In this way, the current ripple will be small, which is beneficial to reduce the torque ripple. When the rotor position exceeds the turn-off angle, the power device adopts hard chopping, which can cause the phase current to drop rapidly and avoid generating a negative torque.

A current look-up table is used to convert the reference torque into the reference current. Due to the memory limitation of 28335DSP, the current look-up table is constructed as a 46×21 table, and the current loop uses an incremental PID algorithm. In the experiment, the parameters of the PI speed controller are set to k_P=0.003, k_I=5e-7 and the parameters of the current controller are set to k_P=3, k_I=0.5. The opening angle θ_{on}=5° , the overlap period θ_{ov}=9° and the turn-off angle θ_{off}=35° are used. The independent channels of Dlog files in CCS software are used to collect data points (each channel can collect 1024 data points), and then MATLAB is used to draw waveforms. The total torque waveforms of the indirect torque control method and the torque compensation control method at 500RPM are shown in Fig.17 (a) and (b), in which the torque is obtained via the torque model $T(i,\theta)$ identified in Section II. Fig.20 gives the actual A-Phase current waveform at 500RPM under two control methods. The data waveforms of different control methods at the same reference speed can be put together to facilitate a clear contrast.

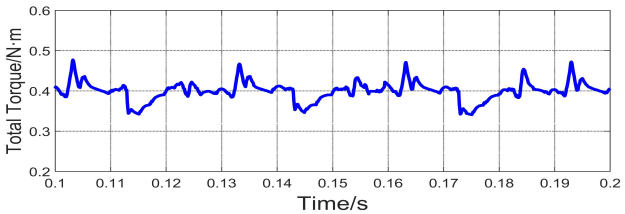

(a) Total torque of indirect torque control

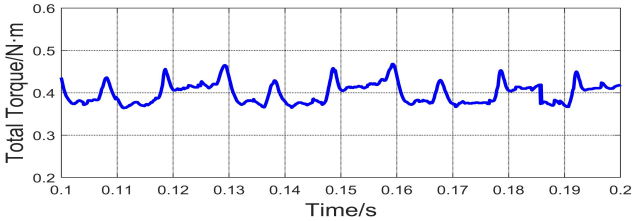

(b) Total torque of torque compensation control

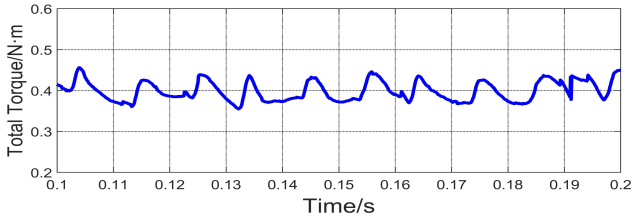

(c) Total torque of DITC

Fig.17. Total torque waveform at 500RPM.

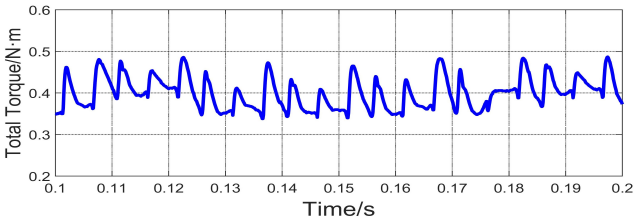

(a) Total torque of indirect torque control

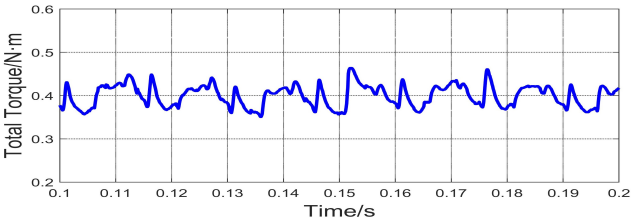

(b) Total torque of torque compensation control

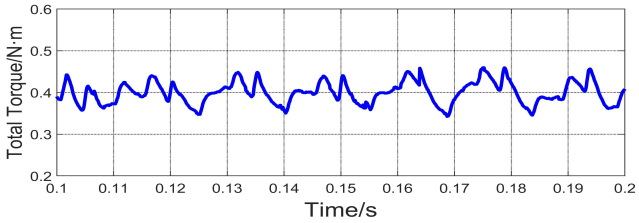

(c) Total torque of DITC

Fig.18. Total torque waveform at 1000RPM.

The subplots (a) and (b) in Fig.18 show the total torque waveform at 1000RPM under indirect torque control and torque compensation control respectively. The actual A-Phase current waveform at 1000RPM under two control methods is shown in Fig.21. The experimental results when the reference speed is 1800RPM are shown in Fig.19 (a), (b) and Fig.22. As shown in Fig.20~22, the torque compensation control strategy can suppress current spikes, which is beneficial to torque ripple reduction.

The direct instant torque control experiment is conducted using the torque model identified in Section II. Since most of the data in the calculation formula are floating-point data, the floating-point to fixed-point code conversion is used to improve the calculation speed. The parameters of the PI speed controller are set to k_P=0.003, k_I=5e-7 and the parameters of the torque controller are set to k_P=5, k_I=0.9. The opening angle θ_{on}=5° , the overlap period θ_{ov}=9° and the turn-off angle θ_{off}=35° are used again. The total torque waveforms under DITC scheme at 500RPM, 1000RPM and 1800RPM respectively are shown in Fig. 17 (c), Fig. 18(c) and Fig. 19 (c).

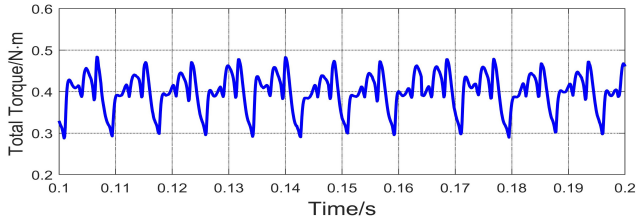

(a) Total torque of indirect torque control

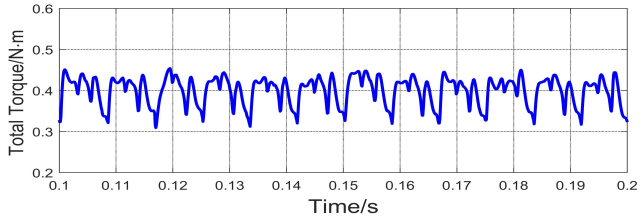

(b) Total torque of torque compensation control

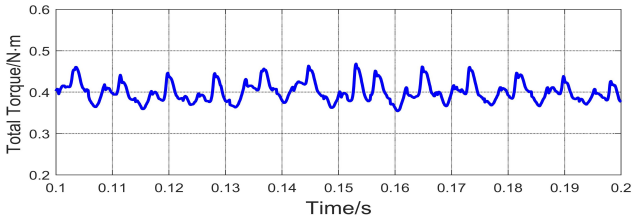

(c) Total torque of DITC

Fig.19. Total torque waveform at 1800RPM.

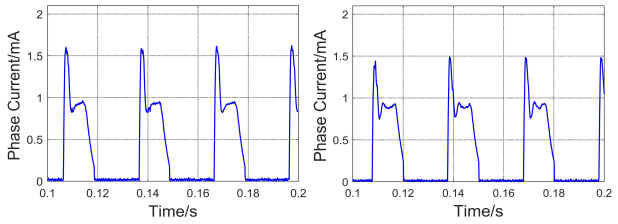

(a) (b)

Fig.20. A-Phase current waveform at 500RPM, (a): indirect torque control; (b): torque compensation control.

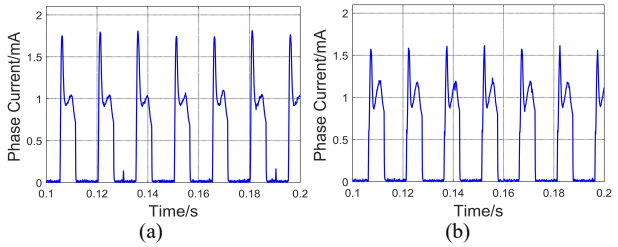

(a) (b)

Fig.21. A-Phase current waveform at 1000RPM, (a): indirect torque control; (b): torque compensation control.

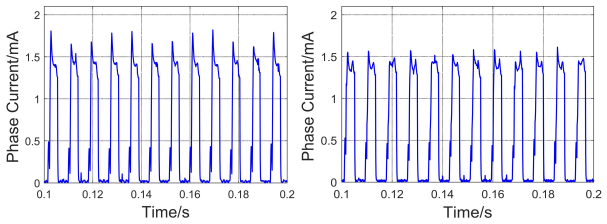

(a) (b)

Fig.22. A-Phase current waveform at 1800RPM, (a): indirect torque control; (b): torque compensation control.

TABLE V
PERFORMANCE COMPARISON OF THE THREE CONTROL METHODS IN THE EXPERIMENT

RPM	*Control Method*	*Torque Ripple Rate (%)*
500	Indirect torque control	32.19
	Torque compensation control	26.05
	DITC	24.32
1000	Indirect torque control	37.23
	Torque compensation control	29.76
	DITC	28.27
1800	Indirect torque control	48.78
	Torque compensation control	36.72
	DITC	29.02

The torque ripple rates of the three methods in experiment are calculated using equation (11). The calculation results are summarized in Table V, which clearly indicates that, the torque ripple of direct instantaneous torque control method or torque compensation control method is significantly smaller than that of the indirect torque control method. The experimental results verify the effectiveness of the two proposed control methods in suppressing torque ripple.

However, it is noted that the torque ripple in experiment has increased, compared with the simulation results. The possible causes are as follows: 1) The three photoelectric sensors used for position detection in the experiment have a low resolution, which affects the realization of TSF control strategy; 2) There are some errors between the established model and the data obtained through FEA, and the floating-point to fixed-point code conversion may also have a negative impact on model accuracy.

V. CONCLUSION

In this paper, two control strategies for torque ripple suppression in SRM have been proposed, based on the Torque-Sharing Function (TSF). One is the torque compensation control strategy, which converts the compensation torque into the compensation current through a current look-up table to reduce current ripple. The other is the direct instantaneous torque control strategy, in which the current loop is replaced by a torque loop to track the reference torque more accurately and reduce torque ripple. These two control schemes have been applied to a switched reluctance motor speed control system, and the experimental results show that the control schemes proposed can effectively reduce the torque ripple generated during the operation of motor. In this paper, the multiple parameters of the identified SRM model hinder the promotion and application of the proposed control strategy, which may be solved by reducing the order of the Fourier function and combining with some modifications of the control algorithms (towards better transient performance) for the speed and torque loops in the future.

REFERENCES

[1] J.D. Widmer, R. Martin, and B.C. Mecrow. “Optimisation of an 80kW

segmental rotor switched reluctance machine for automotive traction," in *Proc. of 2013 IEEE International Electric Machines and Drives Conference*, pp. 427-433, 2013.

[2] J. Ahn, and G.F. Lukman. "Switched reluctance motor: research trends and overview," *CES Transactions on Electrical Machines and Systems*, vol. 2, no. 4, pp. 339-347, Dec. 2018.

[3] K. Aiso, and K. Akatsu. "High speed SRM using vector control for electric vehicle," *CES Transactions on Electrical Machines and Systems*, vol. 4, no. 1, pp. 61-68, Mar. 2020.

[4] L. Henriques, and L. Rolim. "Torque ripple minimization in a switched reluctance drive by neuro-fuzzy compensation," *IEEE Transactions on Magnetics*, vol. 36, no. 5, pp. 3592-3594, Sep. 2000.

[5] C. Choi, S. Kim, Y. Kim, and et al. "A new torque control method of a switched reluctance motor using a torque-sharing function," *IEEE Transactions on Magnetics*, vol. 38, no. 5, pp. 3288-3290, Sep. 2002.

[6] V.P. Vujii. "Minimization of torque ripple and copper losses in switched reluctance drive," *IEEE Transactions on Power Electronics*, vol. 27, no. 1, pp. 388-399, Jan. 2012.

[7] J. Ye, B. Bilgin and A. Emadi, "An extended-speed low-ripple torque control of switched reluctance motor drives," *IEEE Transactions on Power Electronics*, vol. 30, no. 3, pp. 1457-1470, Mar. 2015.

[8] S.K. Sahoo, S.K. Panda and J.X. Xu, "Indirect torque control of switched reluctance motors using iterative learning control," *IEEE Transactions on Power Electronics*, vol. 20, no. 1, pp. 200-208, Jan. 2005.

[9] X.D. Xue, K. Cheng and S.L. Ho. "Optimization and evaluation of torque-sharing functions for torque ripple minimization in switched reluctance motor drives," *IEEE Transactions on Power Electronics*, vol. 24, no. 9, pp. 2076-2090, Sep. 2009.

[10] N. Chayopitak, R. Pupadubsin, K. Tungpimolrut, and etal. "An adaptive low-ripple torque control of switched reluctance motor for small electric vehicle," in *Proc. of 2008 International Conference on Electrical Machines and Systems*, pp. 3327-3332, 2008.

[11] N.T. Shaked, and R. Rabinovici. "New procedures for minimizing the torque ripple in switched reluctance motors by optimizing the phase-current profile," *IEEE Transactions on Magnetics*, vol. 41, no. 3, pp. 1184-1192, Mar. 2005.

[12] R. Mikail, I. Husain, Y. Sozer, and et al. "Torque-ripple minimization of switched reluctance machines through current profiling," *IEEE Transactions on Industry Applications*, vol. 49, no. 3, pp. 1258-1267, May. 2013.

[13] Z. Xia, B. Bilgin, S. Nalakath and et al. "A new torque sharing function method for switched reluctance machines with lower current tracking error," *IEEE Transactions on Industrial Electronics*, vol. 68, no. 11, pp. 10612-10622, Oct. 2020.

[14] X.D. Xue, K.W.E. Cheng, and S.L. Ho. "Simulation of switched reluctance motor drives using two-dimensional bicubic spline," *IEEE Power Engineering Review*, vol. 17, no. 4, pp. 471-477, Dec. 2002.

[15] H.J. Chen, D.Q. Jiang, J. Yang, and et al. "A new analytical model for switched reluctance motors," *IEEE Transactions on Magnetics*, vol. 45, no. 8, pp. 3107-3113, Aug. 2009.

[16] H.P. Chi, R.L. Lin, and J.F. Chen. "Simplified flux-linkage model for switched-reluctance motors," *IEE Proceedings of Electric Power Applications*, vol. 152, no. 3, pp. 577-583, May 2005.

[17] R. Zhong, Y.P. Cao, X.U. Yu-Zhe, and et al. "Analytical model of flux-linkage for switched reluctance motor with trigonometric function," *Electric Machines and Control*, vol. 17, no. 1, pp.13-19, Jan. 2013. (in Chinese)

[18] X. Sun, K. Diao, G. Lei, and et al. "Direct torque control based on a fast modeling method for a segmented-rotor switched reluctance motor in HEV application," *IEEE Journal of Emerging and Selected Topics in Power Electronics*, vol. 9, no. 1, pp. 232-241, Feb. 2021.

[19] M.Divandari, B.Rezaie, and A.Rn. "Improved analytical nonlinear model for switched reluctance motor using gaussian distribution probability density function," *Iranian Journal of Science and Technology, Transactions of Electrical Engineering*, vol. 42, no. 3, pp.343-356, Jun. 2018.

[20] X.D.Xue, K.W.E.Cheng, and S.L.Ho. "A self-training numerical method to calculate the magnetic characteristics for switched reluctance motor drives," *IEEE Transactions on Magnetics*, vol. 40, no. 2, pp. 734-737, Mar. 2004.

Tong Chen received the B.S. degree from the Nanyang Institute of Technology, Nanyang, China, in 2019. He is studying for M.S. degree at the College of Electrical Engineering and Automation, Fuzhou University, Fuzhou, China. His research interests include data modeling and motor control.

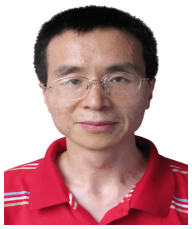

Guoyang Cheng received the B.Eng. degree in information systems from the National University of Defense Technology, Changsha, China, in 1992, the M.Eng. degree in control engineering from Tsinghua University, Beijing, China, in 1995, and the Ph.D. degree from the National University of Singapore (NUS), Singapore, in 2006. Since 2006, he has been with the College of Electrical Engineering and Automation, Fuzhou University, Fuzhou, China, where he is now a professor. His research interests include motion control and mechatronics systems.